Deformation and adiabatic heating of single crystalline and nanocrystalline Ni micropillars at high strain rates

Nidhin George Mathews[1,a], Matti Lindroos[2], Johann Michler[3], Gaurav Mohanty[1]

[1] *Materials Science and Environmental Engineering, Tampere University, Korkeakoulunkatu 6, Tampere 33720, Finland.*

[2] *VTT Technical Research Centre of Finland Ltd, Tekniikantie 21, Espoo 02044, Finland.*

[3] *Laboratory of Mechanics of Materials and Nanostructures, Empa, Swiss Federal Laboratories for Materials Science and Technology, Feuerwerkerstrasse 39, Thun 3602, Switzerland.*

[a] *Corresponding author: nidhin.mathews@tuni.fi*

Abstract

The deformation behavior of single crystal and nanocrystalline nickel were studied with *in situ* micropillar compression experiments from quasi-static to high strain rates up to 10^3/s. Deformation occurred by dislocation slip activity in single crystal nickel whereas extensive grain boundary sliding was observed in nanocrystalline nickel, with a shift towards more inhomogeneous, localized deformation above 1/s. The overall strain rate sensitivity was observed to be nearly two times in nanocrystalline nickel compared to single crystal, as expected. Crystal plasticity based finite element modeling was used to estimate the adiabatic heating, spatially resolved within pillar, at the highest tested strain rates. The simulations predicted a significant temperature rise up to ~ 200 K in nanocrystalline Ni at the grain boundaries and ~ 20 K in single crystalline Ni, due to strain localization. The strain rate sensitivity exponent was observed to remain roughly constant over the tested strain rate range suggesting no change in deformation mechanisms.

Keywords: Nickel, high strain rate, micropillar compression, strain rate sensitivity, adiabatic heating, crystal plasticity

1 Introduction

The mechanical response of materials at high strain rates is a matter of great concern and of immense scientific interest for various engineering applications where impact loading conditions prevail, for e.g. in automobile crash testing and aerospace applications. Macroscale high strain rate (HSR) testing is generally performed with ballistic devices such as split-Hopkinson/Kolsky bar setups for uniaxial tests with speeds up to 100 m/s [1,2]. Moderately high strain rates can be achieved with servo-hydraulic testers reaching up to speeds of 10 m/s. In addition, Charpy and Izod impact testers are used for determining the fracture behavior and impact resistance at moderately high strain rates. However, all these tests provide an averaged microstructural response which is not enough to study the influence of grain anisotropy and influence of grain boundaries. Unlike quasi-static strain rate tests, it is not straightforward to apply digital image correlation on speckle patterns to study the local evolution of strains in high lateral resolutions inside grains and along grain boundaries with split-Hopkinson pressure bar (SHPB) tests due ultra-high speeds of testing. Investigating the response of individual phases, grain orientations and grain boundaries of bulk materials becomes necessary for developing reliable multi-scale models to optimize phase distribution and microstructure for impact applications. Also, with increasing degree of miniaturization, it becomes necessary to

perform small scale, high strain rate tests to assess the impact resistance and crash worthiness of thin films and micro-electro-mechanical systems (MEMS) to design durable devices.

Nanoindentation is the most widely used small scale mechanical testing technique due to minimal sample preparation, offering the possibility to perform hundreds of repeats on the same sample and offering high lateral, depth and temporal resolution mechanics data. It has traditionally been confined to quasi-static strain rates (typically from 10^{-4}/s to 1/s). Although nanoindentation impact tests have existed for close to three decades, these tests are not constant strain rate tests, like their macroscale counterparts, and suffer from rapidly decreasing indentation strain rate with depth [3,4]. This makes the assignment of an effective strain rate and the determination of the corresponding hardness value somewhat unreliable. Also, pyramidal indentation, with large stress gradients, can potentially result in fundamentally different deformation mechanisms than those expected under uniaxial stresses. For e.g. Zhang et al. reported extensive grain boundary formation in aluminum in high strain rate nanoindentation impact tests [5]. Micropillar compression tests, performed with a nanoindenter using a flat punch tip geometry, allow probing uniaxial response at small length scales. Recent developments in nanoindentation hardware and control software capabilities have pushed the envelope of high strain rate testing up to ~ 1000/s [6–8] by overcoming resonance issues at high speeds. In this study, we report micropillar compression data on single crystal (sx) and nanocrystalline (nc) Ni covering 6 orders of strain rates from 10^{-3}/s to 10^{3}/s. The choice of Ni is motivated by face centered cubic (FCC) crystal structure, ease of availability of a microstructurally stable nanocrystalline form through electrodeposition and relatively high yield strength among FCC metals which promotes large adiabatic heating.

It is well known at macro-length scales that a fraction of the input mechanical work is converted to heat during high strain rate testing. Because of the short duration of such tests, the heat produced during the process is not dissipated fast enough to the surroundings and is considered to be adiabatic in nature. The extent of adiabatic heating in high strain rate tests is typically studied using the Taylor-Quinney coefficient (β), which provides the fraction of plastic work that gets converted to heat during rapid deformation of the material [9]. The Taylor-Quinney coefficient has been shown to reach values of ~ 0.9 for strain rates > 1000/s and temperature increase of > 50 ºC reported in some FCC metals [10–12]. Specifically, temperature increase of 5 - 70 ºC was reported for FCC copper at strain rates above 1000/s [10,13]. Soares et al. reported a Taylor-Quiney coefficient change from 0.6 to 0.9 in FCC copper during the strain rate change from 1300/s to 3100/s [13]. Such large adiabatic heating can influence the thermally activated deformation processes, such as dislocation nucleation, glide and cross-slip, and strain hardening [14]. It can also promote microstructural changes in the deforming volume like grain growth. Although high strain rate associated adiabatic heating is reasonably well documented at macroscale testing using high-speed thermal cameras, there are very few estimates of adiabatic heating at microscale for e.g. in nanoindentation and micropillar compression. Since the tested volumes are typically micrometer-cubed, it is not possible to study adiabatic heating using conventional methods like infrared cameras. Therefore, existing literature on microscale testing typically reports estimates of adiabatic heating based on simple analytical and numerical models. Ramachandramoorthy et al. estimated temperature rise of 110 ºC in fused silica glass micropillar compression at 1000 /s using thermal finite element simulations [15]. No such estimates exist for microscale compression in metals, to the best of our knowledge. To fill this critical gap, we utilize comprehensive finite element-based, crystal plasticity modeling (CP-FEM) on single crystal and nanocrystalline FCC Ni that uses experimental micropillar data. Taylor-Quinney coefficient estimates from bulk scale tests are used to predict the extent of adiabatic heating in high strain rate microcompression. The novelty of the reported CP-FEM analysis lies in using

size-dependent micromorphic CP-model with an adiabatic heating model, converting (non-stored) energy to heat at the single and polycrystalline level to provide approximations of temperature rise by simulations, which would be more difficult to obtain experimentally.

This study reports micropillar compression of sx and nc Ni from quasistatic regime (10^{-3}/s to 10^{-1}/s) to high strain rate regime (1/s to 10^3/s) with a focus on studying their deformation behavior and strain rate sensitivity of yield stress, particularly at high strain rates. In addition, a comprehensive CP-FEM model is used to investigate the extent of adiabatic heating in these two materials in microcompression.

2   Materials and methods

2.1   Specimen details

Single crystal Ni sample of (100) plane orientation was purchased from the commercial supplier (MTI Corporation, USA). Nanocrystalline nickel was manufactured using a proprietary electrodeposition technique on silicon wafer. The structural characterization details of the nc Ni sample are reported in a previous work [16]. The silicon wafer was later dissolved in hydrofluoric acid to obtain free standing nc Ni section. The thickness of the free-standing layer was measured to be 0.25 mm. A standard FIB-lamella lift out procedure was performed on the nc Ni sample using the FIB-SEM (Zeiss Crossbeam 540, Germany) to prepare the lamella for the characterization of grain size and texture from transmission Kikuchi diffraction (TKD). The inverse pole figure map determined from TKD (Zeiss Ultraplus, Germany) of the nc Ni sample showed the random orientation of grains with an average grain size of 23 ± 3 nm.

2.2   Micropillar milling and micromechanical testing.

Micropillars of $\sim 3\mu m$ diameter (d) with aspect ratio (l/d) between 3 - 3.5 were fabricated using focused ion beam (FIB) milling (Zeiss Crossbeam 540, Germany) using Ga^+ ions. Ion currents of 7 nA, 3 nA and 300 pA at 30 kV accelerating voltage were used for coarse, intermediate, and fine milling steps respectively in order to progressively reduce Ga^+ implantation damage. Secondary electron (SE) images of micropillars were captured after milling, from which a taper angle less than 2 degrees was measured for all the micropillars. The *in situ* compression of these micropillar samples were performed inside the scanning electron microscope (Zeiss Leo, Germany) using the displacement-controlled indenter (Alemnis AG, Switzerland). Micropillars were compressed uniaxially with a diamond flat punch indenter tip (Synton MDP, Switzerland) of diameter 5 μm up to 20% nominal strain at orders of strain rates ranging from 10^{-3}/s to 10^3/s. Standard load cell assembly was used for micropillar compression in the quasi-static strain rate regime (10^{-3}/s to 10/s), whereas a piezo-based smart-tip load cell assembly was used for HSR regimes (3/s to 1000/s) [8]. The cross-sectional area at the top of the pillar was considered to determine the stresses from the recorded load data, with the flow stress at 1 % strain offset is expressed as the yield strength of the material for all further analysis. The consistency of the yield strength value measured from the standard assembly and the smart-tip assembly was cross-checked at overlapping strain rates of 3/s and 10/s of both setups. The average yield strength value obtained from standard setup was found to be ~ 6 % lower than the smart-tip setup. Therefore, all yield strength values measured from the smart-tip setup were normalized to the standard setup, in order to be consistent with the measurements.

2.3   Crystal plasticity modelling

Size-dependent crystal plasticity model was employed with a micromorphic strain gradient extension. A crystal plasticity model as described in Appendix A was used to investigate low and high strain rate deformation behavior of nickel. Plastic deformation in the FCC Ni is carried

over by twelve octahedral $\{1\,1\,1\}\langle 1\,1\,0\rangle$ slip systems in the model. A sensitivity analysis was performed on adiabatic heating of micropillar and a nano-grained polycrystalline material. The model parameters were identified using low and high strain rate micropillar compression experimental data at 0.01/s and 100/s, respectively. Simulations were performed up to 15 % of strain and the orientation of the compressive loading was [100]. To investigate the adiabatic heating effects in a nano-grained polycrystalline nickel, a polycrystalline simulation case with 200 grains was used. Compression was applied similarly up to around 15 % of axial strain as in the single crystal. Grains were randomly oriented, and the grain size was set to 30 nm. An initial dislocation density of 4.8×10^{15} /m^2 was assigned for the polycrystal. A micropillar fully populated with 30 nm grains is computationally very expensive to investigate, and therefore we used simpler 3D domain for the analysis.

3   Results and Discussion

3.1   Effect of strain rates on the yield strength

The engineering stress-strain response of the sx and nc Ni samples determined from the micropillar compression experiments at various orders of strain rates are shown in Figs 1a and 1b. Both sx and nc Ni showed plastic deformation after the linear elastic behavior. The sx Ni showed typical serrated response in the plastic region due to the avalanche of dislocations with yield strength values ranging between 100 MPa to 200 MPa. The serrated plastic flow due to the avalanches of dislocations is more pronounced at strain rates from 0.001/s to 0.1/s, whereas at strain rates above 1/s, the serrated response gets camouflaged within the noise level. It is to be noted that the micropillar compression experiments of sx Ni is limited up to 100/s strain rate due to low signal to noise ratio. The average yield strength of nc Ni was almost 15 times more than that of sx Ni. These results follow the expected lines of the deformation behavior for both Ni samples [16]. It is observed that the hardening behavior of sx Ni increases with strain rate. On the contrary, the hardening behavior in nc Ni seems to be fairly constant at all strain rates [17]. Due to the inability to accommodate many dislocations inside the nanocrystalline grains and due to constant generation and annihilation of dislocations at the grain boundaries, typically nanocrystalline FCC metals do not exhibit strain hardening. The small hardening in the plastic regime can be considered to be apparent hardening due to geometric taper of the micropillars [18].

The strain rate sensitivity (m) and apparent activation volume (V_{app}) for deformation were calculated using Eq. 1 and Eq. 2 respectively.

$$m = \left[\frac{d(\ln \sigma)}{d(\ln \dot{\varepsilon})}\right]_T \qquad\qquad Eq.\ 1$$

$$V_{app} = \frac{\sqrt{3}kT}{m\,\sigma} \qquad\qquad Eq.\ 2$$

where, σ is the flow stress, $\dot{\varepsilon}$ is the strain rate, k is the Boltzmann constant, T is the absolute temperature.
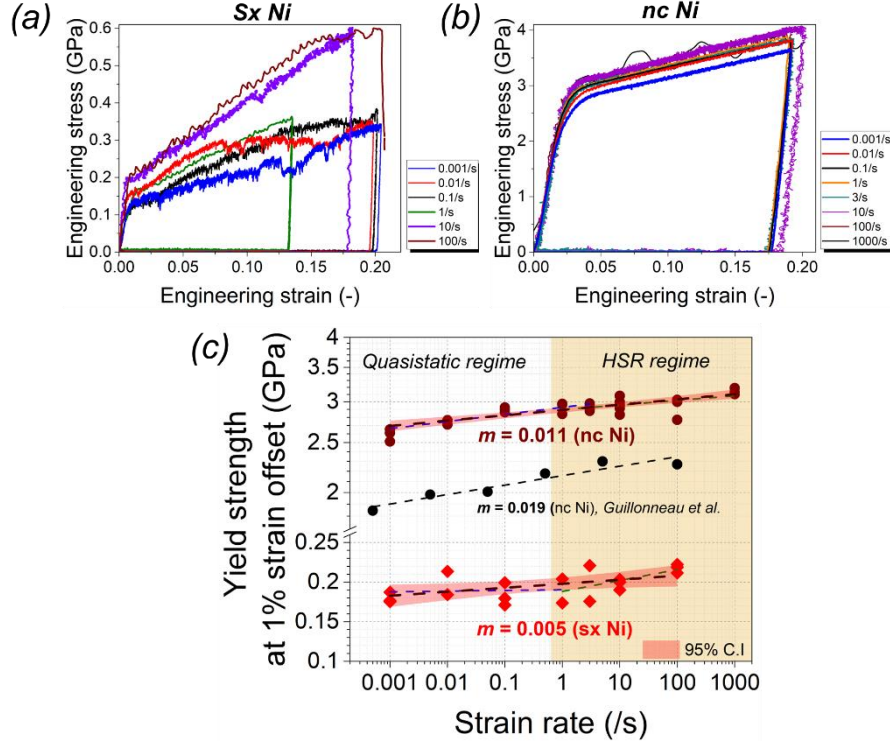
4

Fig 1: Engineering stress-strain curves obtained from micropillar compression at different strain rates for a) sx Ni and b) nc Ni. c) Yield strength values of sx and nc Ni at quasistatic and HSR strain rate regimes with corresponding strain rate sensitivity values. Results from a similar previous work [8] is also replotted for comparison. (Note: Dashed line represents the linear fit of the data points).

The logarithmic plot of yield strength values at 1% strain offset at the corresponding strain rates of deformation is shown Fig 1c. These *m* values obtained from the linear fit of yield strength and strain rate values are plotted for both quasistatic and HSR regimes. The yield strength values of sx Ni show higher scatter compared to nc Ni, this is due to the more stochastic distribution of dislocations in the sx Ni micropillar samples which gets activated during the process of plastic deformation. The strain rate sensitivity of sx Ni is determined to 0.001 in the quasistatic regime and an overall *m* value of 0.005 in the range 0.001/s to 100/s, which is in line with the *m* value of 0.001 from SRJ tests reported in [16]. The overall *m* value is observed to be nearly same as that in the quasistatic regime suggesting same operating deformation mechanisms. Even though the *m* value is estimated to be 0.014 in HSR regime, the data points lie within the scatter range, so that the clear trend cannot be explained explicitly. The insights to the controlling deformation mechanisms can be discussed with the activation volumes calculated from the strain rate sensitivity values using Eq. 2. The apparent activation volume (V_{app}) of ~ $442b^3$ for sx Ni suggests the dislocation glide and possible forest hardening mechanism of deformation. Fig 2a shows the post deformed images of the sx Ni micropillar at both quasistatic and HSR regimes. The sx Ni shows the characteristic slip behavior with distinct slip steps confined to the top 50% of the pillar height at both strain rate regimes. The prominent slip plane is identified to be of the $\{1\,1\,1\}\langle 1\,1\,0\rangle$ type on the surface of the pillar. No considerable differences were observed in slip pattern for sx Ni at all the strain rates selected for compression. This agrees with the constant slope of the yield strength values *vs.* strain rates (in other words strain rate sensitivity) as the deformation mechanism remains unchanged.

The nc Ni sample shows a pronounced strain rate sensitivity with an increasing trend as compared to sx Ni in the quasistatic regime. The *m* value of nc Ni in quasistatic regime was

determined to be 0.014, which is one order of magnitude higher than that of sx Ni. Results from the strain rate jump tests of nc Ni micropillar within this range of strain rates also confirmed the *m* value to be 0.013 (*supplementary information S1*). Beyond 1/s, the yield strength saturates at values closer to 3 GPa, which in effect lowers the *m* value to 0.009. The overall estimated *m* value of 0.011 lies in the range of values previously reported for nanocrystalline Ni with similar grain size [19], which is almost two times than that of sx Ni. No sharp increase in the *m* were observed in our microscale experiments at these strain rates up to 1000/s. This is in line with the results from bulk mechanical testing where there is an abrupt change in the strain rate sensitivity beyond 1000/s [20,21].

The deformation in nc crystal does not exhibit any significant specific slip pattern as observed in sx Ni but showed plastic deformation at the top half of the pillar. The post deformed micropillar images shown in Fig 2b reveals the deformation pattern in nc Ni at strain rates below 0.01/s and above 100/s. In nc Ni, the deformation in the quasistatic regime happens mainly through thermally activated diffusion of atoms and/or nucleation of dislocations along grain boundaries leading to grain boundary sliding or grain boundary rotation. The deformation in the micropillars up to 3 orders of strain rate from 10^{-3}/s to 1/s appears to be more homogenous with majority of the grains in the top half of the pillar contributing to grain boundary sliding. With further increase in the strain rates from 1/s to 100/s the deformation become more localized near the center of the micropillar, which saturates the yield strength to a value of ~ 2.9 GPa. Previous studies suggest extensive dislocation mediated plasticity inside the grains with continuous nucleation and annihilation of dislocations at grain boundaries, which are assisted by grain boundary diffusion. This is in line with ~ $15b^3$ activation volume observed here [16,22,23]. No change in deformation mechanism is observed in the studied strain rate range since the strain rate sensitivity exponent remains constant and no abrupt changes in yield stress are observed at high strain rates. This suggests that the achieved strain rates are not sufficient to suppress grain boundary diffusion processes or go into dislocation drag regimes. One plausible reason can be that the displacement rates of deformation (~10 mm/s at 1000/s) are three orders of magnitude lower compared to bulk scale (>10 m/s at 1000/s). Nanotwinning, grain growth and extensive dislocation entanglements have been reported to dominate the deformation behavior of nc Ni at strain rates of 10^6/s [24], a regime that we clearly do not reach.
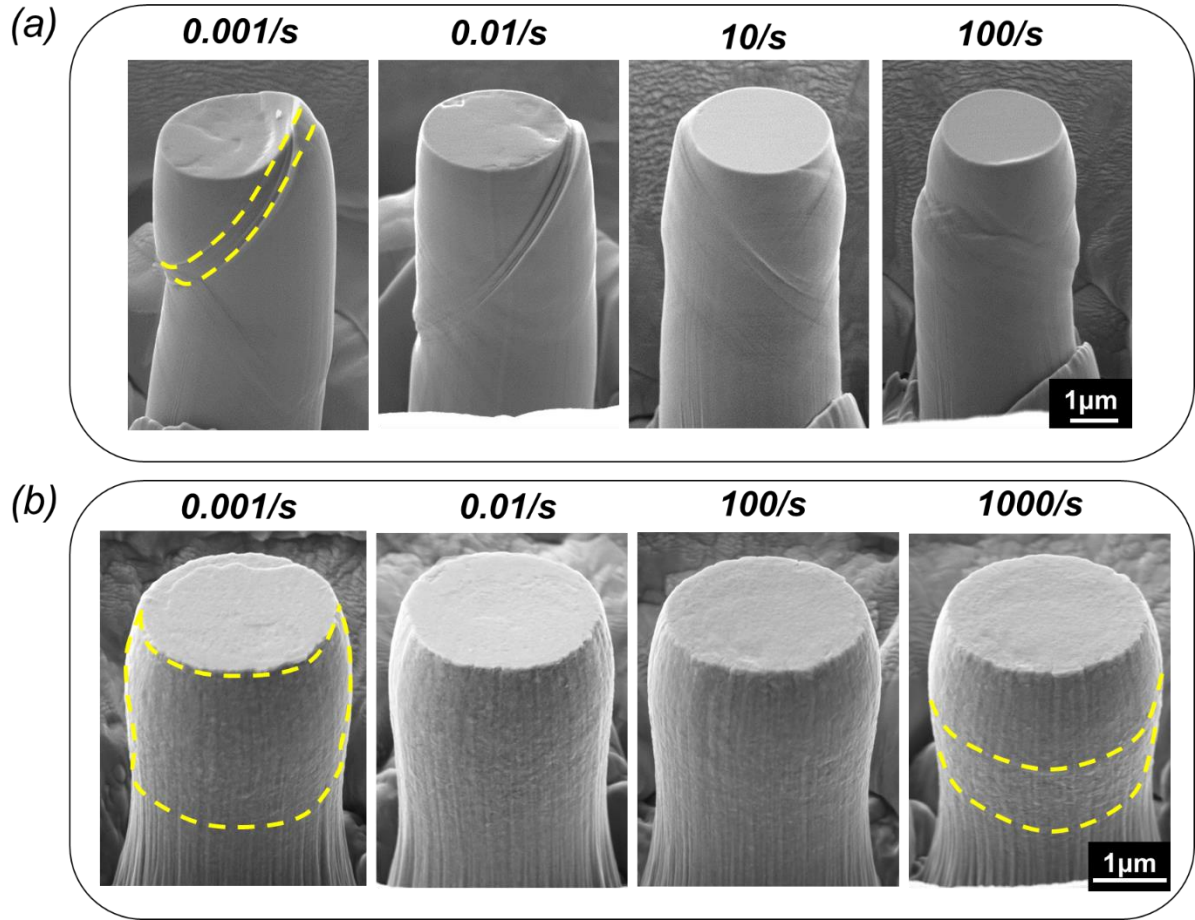
Fig 2: Post deformed micropillars of a) sx nickel, b) nc nickel at quasistatic and HSR strain rate regimes, compressed to 20% nominal strains. (Note: Post compressed images of micropillars for all strain rates tested are added in supplementary information S2 and S3)

3.2 Adiabatic heat evolution at high strain rates

It is seen from Fig 3a that the CP-FE model has a reasonable agreement with the experimental strain rate dependent yield and strain hardening behavior of the sx. It is observed that in the HSR case, the model predicts very similar stress-strain behavior up to large strains irrespective of the taper angle of the micropillar. Fig 3b shows the experimental and simulated stress-strain curves at the strain rate of 100/s and 1000/s for the nc Ni with a high yield stress due to activated Hall-Petch effect in the model. Good agreement between the experiments and simulations are observed. Two different values of Taylor-Quiney coefficients were used to evaluate low and high heat generation at 1000/s, corresponding to values 0.6 and 0.9 for variable β [13]. Effectively, lower β results in higher strain hardening since the CP model response is less affected by the limited temperature rise.

During the micropillar test of sx Ni in the quasistatic regime, it was observed that the apparent strain hardening of the material decreases rapidly, which can be caused by slip localization in the pillar. However, our simulations do not show slip localization in the pillar, which can be due to the assumption that the pillars have identical initial dislocation density for all slip systems which are homogeneously distributed in the pillar. Furthermore, the geometry of the pillar does not contain any irregularities, idealizing the micropillar compression test. Therefore, slip-slip interaction and length-scale regularization by the model does not predict nucleation of slip bands due to the absence of any slip nucleation sites. Instead, the simulation

shows rather ideally distributed contribution from different slip systems for the [100] orientation. Fig 3c shows that the predicted temperature increases in the sx Ni micropillar is close to 20 K at maximum with localized dislocation density as seen in Fig 3d, when assuming fully adiabatic condition for the simulation with Taylor-Quinney coefficient of 0.9. This result suggests that the increase in temperature due to adiabatic heating is not very significant, when notable slip band formation is not observed. Temperature rise can become higher if significant slip localization would occur in the simulations.

Fig. 3e shows the representative volume of the polycrystalline Ni microstructure consisting of approximately 200 grains with a size of ~30 nm used to predict the adiabatic heating effects in nc Ni. The temperature distribution inside the polycrystalline microstructure of Ni at strain rate of 1000/s and $\beta = 0.9$ is shown in Fig. 3f (legend limited to 200 K increase). Significant temperature rise ranging generally between 30 to 170 K is observed, whereas the peak temperature value exceeding 200 K locally are predicted by the model at some hotspots near grain boundaries at 15% of axial strain (see *supplementary information S4* for the distribution of temperature change inside grains). However, the model does not account for the extensive grain boundary sliding observed in the experiments, which would have further reduced the temperatures at these grain boundary hotspots. These hotspots also show very high dislocation density in the deformed state (Fig. 3g) due to local temperature induced softening in the material behavior. Temperature dependent annihilation of dislocations is not sufficient to suppress the multiplication process with the identified model parameters. Generally, however, the temperature increase in the material can be judged to 70-150 K in majority of the grains, excluding grain boundary hotspots. Therefore, the simulations indicate that it is plausible that the temperature increase in polycrystalline micropillar test at high strain rates can become very significant locally.
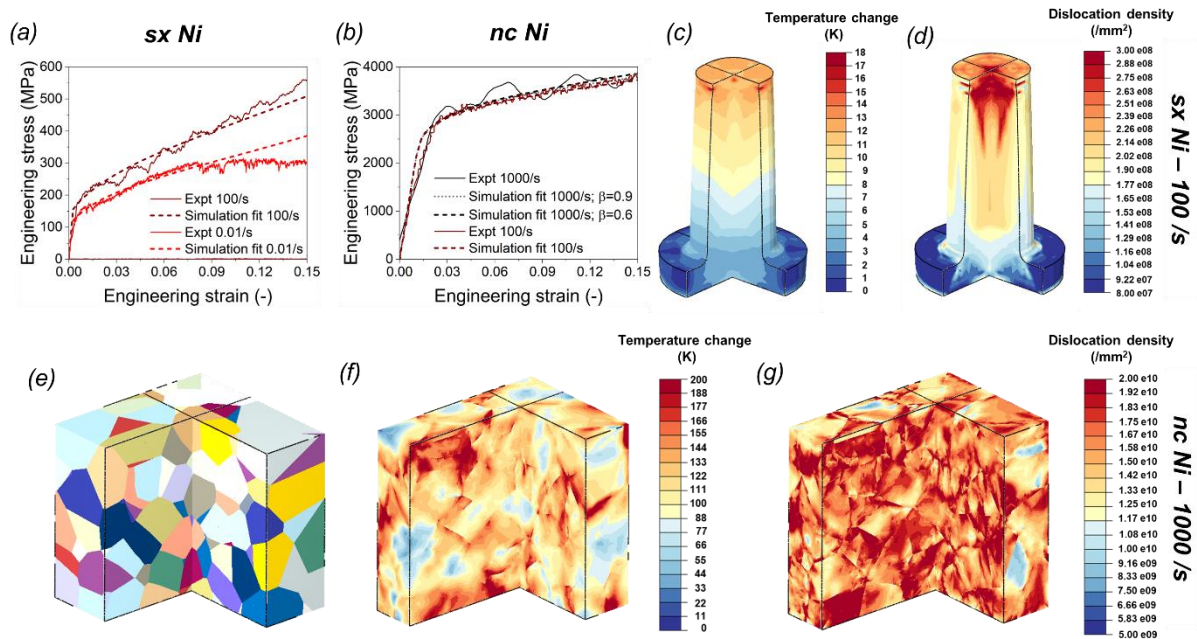

Figure 3: a) Stress-strain comparison of simulations and experiments up to 15% nominal strain in a) sx Ni at the strain rates of 0.01 and 100/s, b) nc Ni at the strain rate of 1000/s. c) Distribution of temperature increase and d) dislocation density in sx Ni at 100/s compression to 15% nominal strain for β = 0.9. e) Representative volume of the used polycrystalline microstructure of nc Ni. f) Distribution of temperature increase and g) dislocation density in nc Ni at 1000/s compression to 15% nominal strain for β = 0.9.

Even though the temperature increase was found to be up to ~ 200 K at grain boundaries at 1000/s, no noticeable grain growth was observed in the nc Ni sample tested at 1000/s from TKD analysis (Fig. 4a). The grain size distribution of the undeformed and deformed regions from a micropillar compressed at 1000 /s and up to ~ 20% strain is shown in Fig. 4b. The average grain size remains roughly the same in both cases suggesting no microstructural changes in nc Ni due to adiabatic heating.
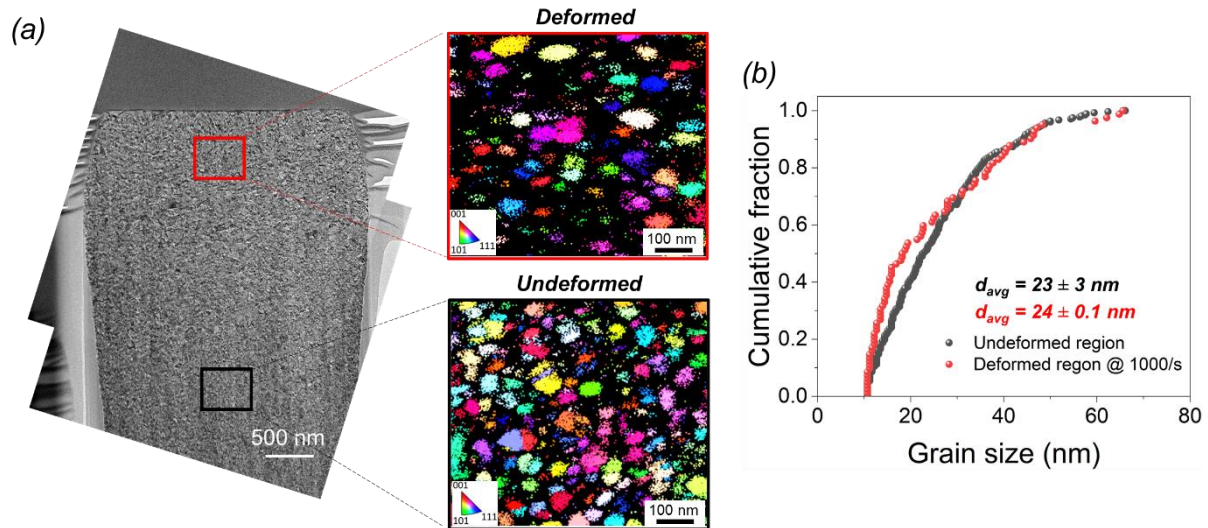

Fig 4: a) Overview of deformed nc Ni micropillar with the IPF maps in the undeformed and deformed regions (Note: Locations of TKD scans are marked in the squares). b) Grain size distribution in the undeformed and deformed region of nc Ni from TKD analysis.

4   Conclusions

The deformation response of sx and nc Ni were studied at various orders of strain rates (10^{-3}/s – 10^3/s) using micropillar compression experiments. The overall strain rate sensitivity values were estimated to be 0.005 for sx Ni and 0.011 for nc Ni. The dislocation glide deformation mechanisms dominated in sx Ni whereas grain boundary assisted deformation operated in nc Ni. The deformation in nc Ni at 1000/s strain rates is observed to be more inhomogeneous and localized, whereas the homogenous deformation is seen in quasistatic strains rates. The performed crystal plasticity simulations do not indicate very high temperature rise in single crystal micropillars deformed at high strain rates. However, nanocrystalline Ni can exhibit temperature rises upto 200 K locally near grain boundaries based on the simulations assuming adiabatic conditions at strain rates of 1000/s. No grain growth was observed in nanocrystalline Ni samples due to the temperature rise as a result of adiabatic heating effects.

CRediT authorship contribution statement

Nidhin George Mathews: Conceptualization, Data curation, Formal Analysis, Investigation, Methodology, Visualization, Writing – original draft, Writing – review & editing. **Matti Lindroos:** Formal Analysis, Investigation, Writing – original draft, Writing – review & editing. **Johann Michler:** Writing – review & editing. **Gaurav Mohanty:** Conceptualization, Supervision, Funding acquisition, Writing – review & editing.

Declaration of Competing Interest

The authors declare that they have no known competing financial interests or personal relationships that could have appeared to influence the work reported in this paper.

Acknowledgements

References

[1] B. Hopkinson, Philosophical Transactions of the Royal Society of London. Series A, Containing Papers of a Mathematical or Physical Character 213 (1913) 437–456.

[2] H. Kolsky, Proc. Phys. Soc. B 62 (1949) 676.

[3] J.M. Wheeler, J. Dean, T.W. Clyne, Extreme Mechanics Letters 26 (2019) 35–39.

[4] M. Rueda-Ruiz, B.D. Beake, J.M. Molina-Aldareguia, Materials & Design 192 (2020) 108715.

[5] Y. Zhang, B.L. Hackett, J. Dong, K.Y. Xie, G.M. Pharr, Proceedings of the National Academy of Sciences 120 (2023) e2310500120.

[6] P. Sudharshan Phani, W.C. Oliver, Materials 10 (2017) 663.

[7] C. Zehnder, S. Bruns, J.-N. Peltzer, K. Durst, S. Korte-Kerzel, D. Möncke, Front. Mater. 4 (2017).

[8] G. Guillonneau, M. Mieszala, J. Wehrs, J. Schwiedrzik, S. Grop, D. Frey, L. Philippe, J.-M. Breguet, J. Michler, J.M. Wheeler, Materials & Design 148 (2018) 39–48.

[9] G.I. Taylor, H. Quinney, Proceedings of the Royal Society of London. Series A, Containing Papers of a Mathematical and Physical Character 143 (1997) 307–326.

[10] D. Rittel, A.A. Kidane, M. Alkhader, A. Venkert, P. Landau, G. Ravichandran, Acta Materialia 60 (2012) 3719–3728.

[11] D. Rittel, L.H. Zhang, S. Osovski, Journal of the Mechanics and Physics of Solids 107 (2017) 96–114.

[12] N.I. Vazquez-Fernandez, G.C. Soares, J.L. Smith, J.D. Seidt, M. Isakov, A. Gilat, V.T. Kuokkala, M. Hokka, J. Dynamic Behavior Mater. 5 (2019) 221–229.

[13] G.C. Soares, M. Hokka, International Journal of Impact Engineering 156 (2021) 103940.

[14] A. Eisenlohr, I. Gutierrez-Urrutia, D. Raabe, Acta Materialia 60 (2012) 3994–4004.

[15] R. Ramachandramoorthy, J. Schwiedrzik, L. Petho, C. Guerra-Nuñez, D. Frey, J.-M. Breguet, J. Michler, Nano Lett. 19 (2019) 2350–2359.

[16] J. Wehrs, G. Mohanty, G. Guillonneau, A.A. Taylor, X. Maeder, D. Frey, L. Philippe, S. Mischler, J.M. Wheeler, J. Michler, JOM 67 (2015) 1684–1693.

[17] J.R. Trelewicz, C.A. Schuh, Acta Materialia 55 (2007) 5948–5958.

[18] G. Mohanty, J.M. Wheeler, R. Raghavan, J. Wehrs, M. Hasegawa, S. Mischler, L. Philippe, J. Michler, Philosophical Magazine 95 (2015) 1878–1895.

[19]   Q. Wei, J Mater Sci 42 (2007) 1709–1727.

[20]   R.T. Humphrey, A.F. Jankowski, Surface and Coatings Technology 206 (2011) 1845–1849.

[21]   S. Rajaraman, K.N. Jonnalagadda, P. Ghosh, in: V. Chalivendra, B. Song, D. Casem (Eds.), Dynamic Behavior of Materials, Volume 1, Springer, New York, NY, 2013, pp. 157–163.

[22]   M.A. Meyers, A. Mishra, D.J. Benson, Progress in Materials Science 51 (2006) 427–556.

[23]   J. Schwiedrzik, R. Ramachandramoorthy, T.E.J. Edwards, P. Schürch, D. Casari, M.J. Duarte, G. Mohanty, G. Dehm, X. Maeder, L. Philippe, J.-M. Breguet, J. Michler, Materials & Design 220 (2022) 110836.

[24]   Z. Jiang, Q. Wang, Y. Zhang, T. Suo, J. Wang, J. Liang, Materials Letters 305 (2021) 130790.

Appendix A

Deformation and adiabatic heating of single crystalline and nanocrystalline Ni micropillars at high strain rates

Nidhin George Mathews[1,a], Matti Lindroos[2], Johann Michler[3], Gaurav Mohanty[1]

[1] *Materials Science and Environmental Engineering, Tampere University, Korkeakoulunkatu 6, Tampere 33720, Finland.*

[2] *VTT Technical Research Centre of Finland Ltd, Tekniikantie 21, Espoo 02044, Finland.*

[3] *Laboratory of Mechanics of Materials and Nanostructures, Empa, Swiss Federal Laboratories for Materials Science and Technology, Feuerwerkerstrasse 39, Thun 3602, Switzerland.*

[a] *Corresponding author: nidhin.mathews@tuni.fi*

Size-dependent crystal plasticity model was employed with a micromorphic strain gradient extension. Finite strain formalism was used with decomposition of deformation gradient to elastic and plastic parts, $\underline{F} = \underline{F}^E \cdot \underline{F}^P$. Plastic deformation in the FCC material is carried over by twelve octahedral {111} <110> slip systems in the model. A dislocation density-based formulation is utilized, and it shares similarities for an FCC model suggested by Monnet et al. [1]. Plastic velocity gradient in computed as a sum over all slip systems $\underline{L}^p = \sum_{s=1}^{N_s} \dot{\gamma}^s \underline{N}^s$, where $\underline{N}^s$ is the orientation tensor of a slip system *s*. Slip rate of a dislocation slip system *s* is given by a Norton type of flow rule:

$$\dot{\gamma}^s = \left\langle \frac{|\tau^s| - \tau_c}{K} \right\rangle^N sign(\tau^s)$$

where τ^s is the resolved shear stress of a slip system computed with $\tau^s = \left(\underline{C}^E \cdot \left(\underline{\Lambda} : \underline{E}_{GL} \right) \right) : \underline{N}^s$, where $\underline{C}^E$ is the Cauchy-Green tensor, $\underline{\Lambda}$ stiffness tensor, and $\underline{E}_{GL}$ Green-Lagrange strain tensor. Parameters K and N describe viscosity and strain rate dependency, respectively. Slip resistance of a slip system is defined as:

$$\tau_c^s = \tau_0 + \tau_{HP} + \mu b^s \sqrt{\sum_{s=1}^{N_s} a_{eff}^s \rho^s} - S_\chi$$

where $\tau_{HP} = \frac{\mu}{\mu_{RT}} \frac{K}{\sqrt{d}}$ is the Hall-Petch effect. Coefficient K is a Hall-Petch constant and effective grain size is denoted with d. The Hall-Petch effect in the model is scaled with a temperature dependent shear modulus μ with respect to room temperature shear modulus μ_{RT}. Solid solution strengthening term τ_0 is assumed to be zero for the pure metal and the slip resistance of the material is dependent on the initial dislocation density and the related interactions between slip systems. Generalized stress is included in the model using reduced micromorphic formulation as described in detail in [2–4]. The model introduces size effects on the material model and regularizes slip localization. The generalized stress is defined as

$$S_\chi = -H_\chi(\gamma_{cum} - \gamma_\chi) = A\Delta_\chi \gamma_\chi$$

where two length-scale parameters are introduced H_χ and A. Cumulative plastic slip is computed by $\gamma_{cum} = \int_0^t \sum_{s=1}^{N_s} |\dot{\gamma}^s|\, dt$.

The dislocation interactions coefficients are not constant in the model, and they evolve similarly as suggested in [1].

$$a_{eff}^s = \left(0.2 + 0.8 \frac{\ln\left(b^s \sqrt{\sum_{s=1}^{N_s} a_{const}^S \rho^s}\right)}{\ln\left(b^s \sqrt{\rho_{ref}}\right)} \right)^2 a_{const}^s$$

Dislocation density evolution is described with:

$$\dot{\rho}^s = \frac{|\dot{\gamma}^s|}{b^s} \left[\frac{1}{d} + \frac{\sqrt{\sum_{forest} a_{eff}^s \rho^s}}{K_{forest}} + \frac{\sqrt{\sum_{coplan} a_{eff}^s \rho^s}}{K_{coplan}} - y\rho^s \right]$$

where hardening related parameters K_{forest} and K_{coplan} describe the number of obstacles overcome by dislocations on average before becoming immobile. Dislocation annihilation is formulated with temperature and strain rate dependent distance y [5].

$$y = 2\, y_0 \left(1 - \frac{k_B T}{A_{rec}} \ln\left|\frac{\dot{\gamma}^s}{\dot{\gamma}_0}\right| \right)$$

where y_0 is reference annihilation distance, A_{rec} is the capture radius energy, and $\dot{\gamma}_0$ a reference slip rate. Adiabatic heat generation and the related increase rate in temperature is similar to [4,6], but modified for the micromorphic model.

$$\dot{T} = \frac{\beta\left(\sum_{s=1}^{N_s} \tau^s \dot{\gamma}^s + S_\chi \gamma_{cum}\right)}{\rho c}$$

where β is the Taylor-Quinney coefficient (assumed constant 0.9 here), ρ is the mass density, and c material's heat capacity. It is assumed in this work that at the strain rate of 100/s the condition is fully adiabatic. Thermal strains will build up in the material due to uneven heating, however, their effect is omitted in the current study for simplicity. Table 1 list the used crystal plasticity parameters.

Table 1: Crystal plasticity parameters used in the simulations.

Parameters	Value	Unit
Elastic constant (C_{11})	$248.33 \cdot 10^3 - 51.07 \cdot T$	MPa
Elastic constant (C_{12})	$151.2 \cdot 10^3 - 12.77 \cdot T$	MPa
Elastic constant (C_{44})	$125.7 \cdot 10^3 - 44.39 \cdot T$	MPa
Shear modulus (μ)	$\sqrt{C_{44}\left(\dfrac{C_{11} - C_{12}}{C_{22}}\right)}$	MPa
Viscous parameter (K)	18.0	$MPa.s^{1/N}$

Strain rate exponent (N)	12.0	-
Hall-Petch coefficient (K_{HP}))	3.7944 (polycrystal), 0.0 (micropillar)	$MPa/\sqrt{mm}$
Grain size (d)	30 nm (polycrystal), and the average diameter of the micropilar (micropilar)	μm
Length of Burgers vector (b^s)	0.254	nm
Interaction coefficients (a_i)	$a_1 = 0.124, a_2 = 0.124, a_3 = 0.07,$ $a_4 = 0.625, a_5 = 0.137, a_6 = 0.122$	-
Annihilation distance (reference) (y_0)	$5 \cdot b^s$	nm
Capture radius energy (A_{rec})	2E-20	J
Reference slip rate ($\dot{\gamma}_0$)	1E7	s^{-1}
Forest hardening parameter	70	-
Coplanar hardening parameter	150	-
Length-scale penalty modulus (H_χ)	2000	$MPa.mm^2$
Length-scale parameter (A)	0.008	N
Mass density (ρ)	8830	kg/m^3
Heat capacity (c)	455	J/K

References

[1] G. Monnet, C. Mai, Journal of Nuclear Materials 518 (2019) 316–325.

[2] C. Ling, S. Forest, J. Besson, B. Tanguy, F. Latourte, International Journal of Solids and Structures 134 (2018) 43–69.

[3] M. Lindroos, J.-M. Scherer, S. Forest, A. Laukkanen, T. Andersson, J. Vaara, A. Mäntylä, T. Frondelius, International Journal of Plasticity 151 (2022) 103187.

[4] Tom. Andersson, Matti. Lindroos, Rami. Pohja, Abhishek. Biswas, Supriya. Nandy, Janne. Pakarinen, Juhani. Rantala, Materials at High Temperatures 41 (2024) 51–60.

[5] S. Lee, H. Cho, C.A. Bronkhorst, R. Pokharel, D.W. Brown, B. Clausen, S.C. Vogel, V. Anghel, G.T. Gray, J.R. Mayeur, International Journal of Plasticity 163 (2023) 103529.

[6] V. Phalke, S. Forest, H.-J. Chang, T. Rose, A. Roos, J Mater Sci 59 (2024) 5201–5232.

Supplementary information

Deformation and adiabatic heating of single crystalline and nanocrystalline Ni micropillars at high strain rates

Nidhin George Mathews[1,a], Matti Lindroos[2], Johann Michler[3], Gaurav Mohanty[1]

[1] *Materials Science and Environmental Engineering, Tampere University, Korkeakoulunkatu 6, Tampere 33720, Finland.*

[2] *VTT Technical Research Centre of Finland Ltd, Tekniikantie 21, Espoo 02044, Finland.*

[3] *Laboratory of Mechanics of Materials and Nanostructures, Empa, Swiss Federal Laboratories for Materials Science and Technology, Feuerwerkerstrasse 39, Thun 3602, Switzerland.*

[a] *Corresponding author: nidhin.mathews@tuni.fi*

S1. Strain rate jump tests on nanocrysalline nickel

Strain rate jump tests on nanocrystalline nickel micropillar were performed by varying the strain rate by one order of magnitude for each jump. Fig. S1 shows representative engineeering stress- strain curve for strain jumps between 10^{-1} /s to 10^{-3}/s. The strain rate sensitivity (*m*) value of 0.013 was estimated using Eq. 1 (in the main manuscript).
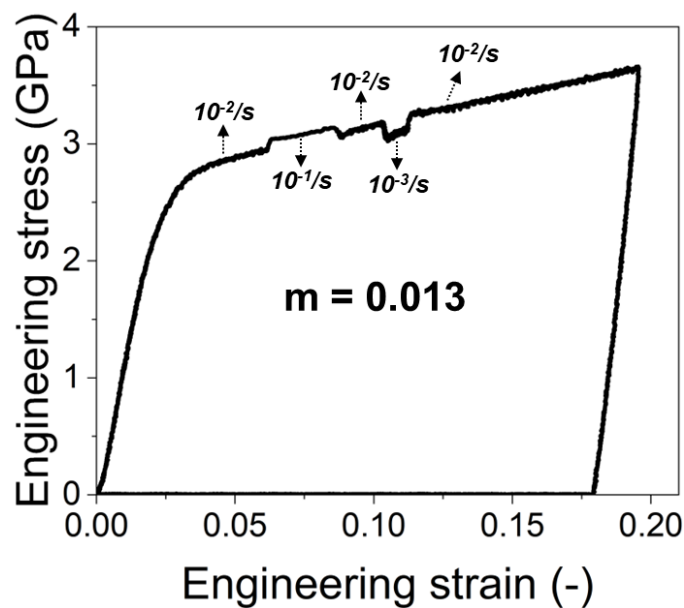

Fig S1: Representative engineering stress-strain curve of strain rate jump tests on nc Ni micropillars

S2. Micropillar compression of sx Ni at different orders of strain rates
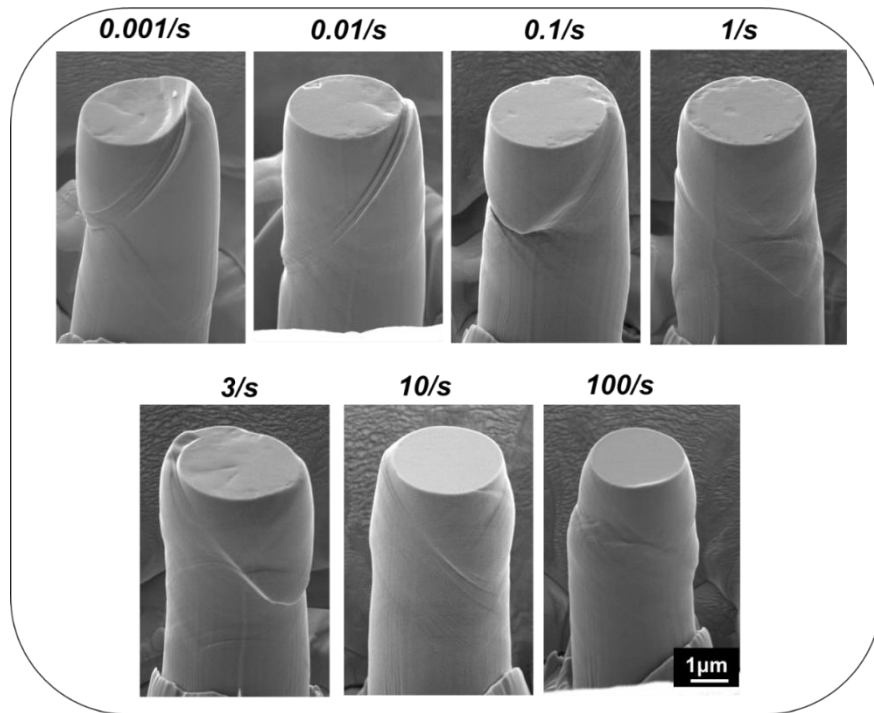

Fig S2: Post-compressed images of sx Ni micropillar at orders of strain rates ranging from 0.001/s to 100/s

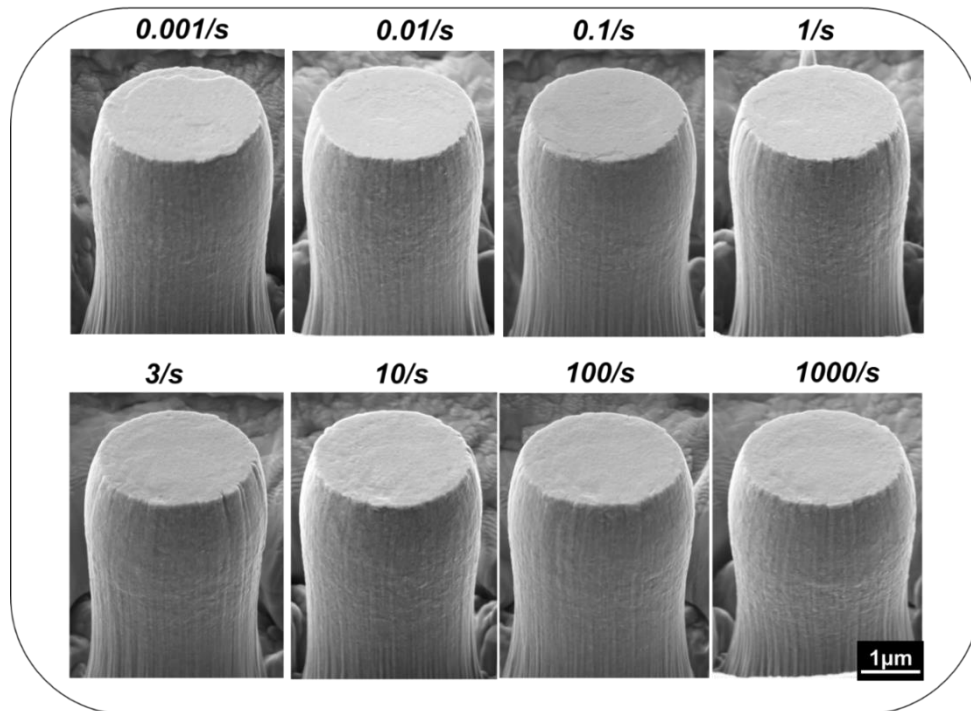**S3. Micropillar compression of nc Ni at different orders of strain rates**

Fig S3: Post-compressed images of nc Ni micropillar at orders of strain rates ranging from 0.001/s to 1000/s

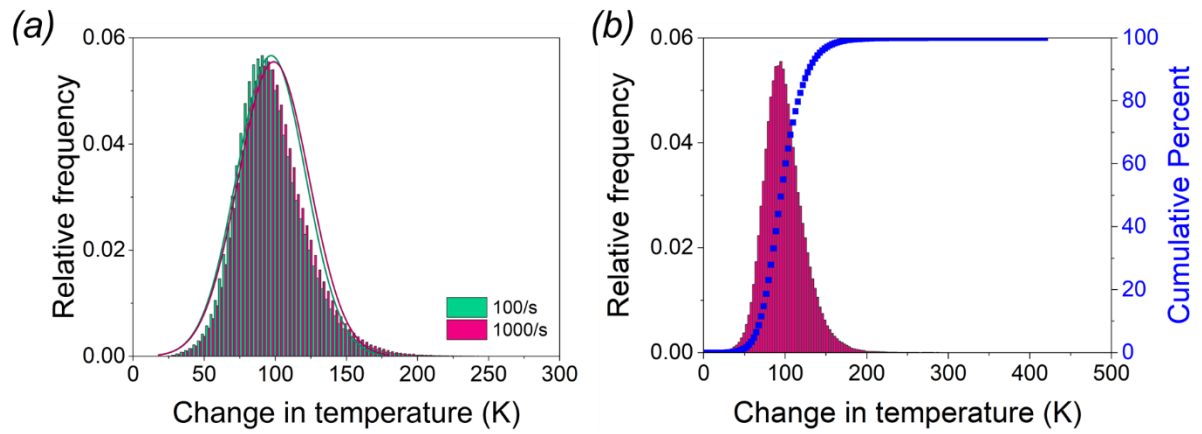**S4. Temperature change inside the nc Ni grains from CP-FEM simulations**

Fig S4: a) Temperature rise distribution inside the nc Ni grain estimated from CP-FEM simulations at 100/s and 1000/s strain rates. b) Cumulative percent of the temperature rise in nc Ni at 1000/s strain rates.